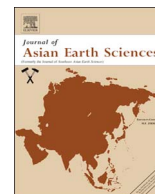# Transient rheology of the oceanic asthenosphere following the 2012 Indian Ocean Earthquake inferred from geodetic data

Cecep Pratama, Takeo Ito, Ryohei Sasajima,

Takao Tabei, Fumiaki Kimata, Endra Gunawan,

Yusaku Ohta, Tadashi Yamashina, Nazli Ismail,

Irwandi Nurdin, Didik Sugiyanto, Umar Muksin,

Irwan Meilano

Full length article

Transient rheology of the oceanic asthenosphere following the 2012 Indian Ocean Earthquake inferred from geodetic data

Cecep Pratama[a,*], Takeo Ito[a], Ryohei Sasajima[b], Takao Tabei[c], Fumiaki Kimata[d], Endra Gunawan[e], Yusaku Ohta[f], Tadashi Yamashina[c], Nazli Ismail[g], Irwandi Nurdin[g], Didik Sugiyanto[g], Umar Muksin[g], Irwan Meilano[h]

[a] Graduate School of Environmental Studies, Nagoya University, Nagoya, Japan
[b] International Institute of Seismology and Earthquake Engineering, Ibaraki, Japan
[c] Department of Applied Science, Kochi University, Akebono-cho, Japan
[d] Tono Research Institute of Earthquake Science, Mizunami, Japan
[e] Graduate Research on Earthquake and Active Tectonics, Bandung Institute of Technology, Indonesia
[f] Graduate School of Science, Tohoku University, Sendai, Japan
[g] Department of Physics, Syiah Kuala University, Banda Aceh, Indonesia
[h] Faculty of Earth Sciences and Technology, Bandung Institute of Technology, Indonesia

ARTICLE INFO

ABSTRACT

Postseismic motion in the middle-field (100–500 km from the epicenter) geodetic data resulting from the 2012 Indian Ocean earthquake exhibited rapid change during the two months following the rupture. This pattern probably indicates multiple postseismic deformation mechanisms and might have been controlled by transient rheology. Therefore, the relative contribution of transient rheology in the oceanic asthenosphere and afterslip in the oceanic lithosphere should be incorporated to explain short- and long-term transitional features of postseismic signals. In this study, using two years of post-earthquake geodetic data from northern Sumatra, a three-dimensional spherical-earth finite-element model was constructed based on a heterogeneous structure and incorporating transient rheology. A rheology model combined with stress-driven afterslip was estimated. Our best-fit model suggests an oceanic lithosphere thickness of 75 km with oceanic asthenosphere viscosity values of 1×10^{17} Pa s and 2×10^{18} Pa s for the Kelvin and Maxwell viscosity models, respectively. The model results indicate that horizontal landward motion and vertical uplift in northern Sumatra require viscoelastic relaxation of the oceanic asthenosphere coupled with afterslip in the lithosphere. The present study demonstrates that transient rheology is essential for reproducing the rapidly changing motion of postseismic deformation in the middle-field area.

1. Introduction

The seismic moment and stress released by great earthquakes cause extensive, long-lasting postseismic deformation within the lithosphere and asthenosphere. Postseismic motion, which can be detected by geodetic observation, may reflect a large contribution of viscoelastic relaxation in the upper mantle (Wang et al., 2012). This mechanism could explain the rheological properties in the mantle, which is fundamental to understand plate tectonics.

On April 11, 2012, a great oceanic earthquake (Mw 8.6) struck off the west coast of northern Sumatra about 150 km west of the Sunda trench and was followed by a great aftershock (Mw 8.2) approximately two hours after the main shock (Satriano et al., 2012; Yue et al., 2012). This sequence, which was the largest instrumentally recorded intraplate earthquake in history, yielded a total seismic moment of approximately $12–13 \times 10^{21}$ and $2–3 \times 10^{21}$ N m for the main shock and aftershock, respectively (Hill et al., 2015; Wei et al., 2013; Yue et al., 2012). Large oceanic intraplate earthquakes are extremely rare and provide valuable opportunities to investigate the rheological properties under the ocean.

Previous studies have explored the rheology of the asthenospheric layer following the 2012 Indian Ocean Earthquake. Based on postseismic gravity changes using Gravity Recovery and Climate

Experiment data, Han et al. (2015) suggested the occurrence of bi-viscous viscoelastic flow with a transient and steady-state viscosity of approximately 1×10^{18} and 1×10^{19} Pa s, respectively. In contrast, based on mid-field and far-field (> 500 km from the epicenter) GNSS data for the three years after the event, Hu et al. (2016) obtained a Maxwell viscosity of approximately 2×10^{18} Pa s with an asthenosphere thickness of 80 km.

These previous analyses obtained different values for the viscosity of the asthenosphere: this discrepancy may have arisen from the complex geometries and different modeling assumptions. Previous studies used different fixed oceanic lithosphere thickness as a prior assumption. However, there is no direct constraint of oceanic lithosphere thickness beneath the Indian Ocean and the oceanic lithosphere thickness may have a significant trade-off with oceanic asthenosphere viscosity. In addition, Hu et al. (2016) apparently failed to explain middle field data where transient motion was observed. In this study, we analyzed the middle field data to obtain oceanic lithosphere thickness and transient rheology beneath the Indian Ocean. Hereinafter, we constructed a three-dimensional spherical-earth finite-element model with a three-dimensional heterogeneous earth velocity structure based on seismic tomography. We used two years of GNSS postseismic displacement data and focused only on mid-field stations in northern Sumatra to provide a strong constraint on viscosity, particularly transient viscosity. Postseismic deformation due to strike-slip earthquakes has been widely modeled as viscoelastic relaxation (Hu et al., 2016), afterslip (Miyazaki et al., 2004), and poroelastic rebound (Peltzer et al., 1998). We did not consider poroelastic rebound because of the limited geodetic network and because the decay time is short (a few weeks) and the rebound has relatively small amplitude. In this study, we combine the other two possible mechanisms (afterslip and viscoelastic relaxation).

2. Data and methods

2.1. Geodetic observation data

We utilized the postseismic displacement based on daily solutions of four sites from the Aceh GNSS Network for the Sumatran fault system (AGNeSS), and one site from the Sumatran GPS Array (SuGAr), all of which are located in northern Sumatra. AGNeSS was developed by Nagoya University, Kochi University, Tohoku University, Institut Teknologi Bandung, and Syiah Kuala University, beginning a couple of months after the 2004 Sumatra–Andaman Earthquake (Ito et al., 2012). Data for the one site from the SuGAr network was obtained from the Scripps Orbit and Permanent Array Center website (http://garner.ucsd.edu). This network is very near to the location and recorded both horizontal and vertical data clearly (Fig. 1). To obtain the surface displacement, we processed each Receiver Independent Exchange format dataset from 2005 to 2014.3 to yield the time history of each GNSS site. The data were processed using BERNESE 5.0 software (Dach et al., 2007) with the permanent International GNSS Service site as a realization in the International Terrestrial Reference frame 2008 (Altamimi et al., 2011).

Each site in northern Sumatra continued to record postseismic deformation after the 2004 Sumatra–Andaman earthquake (Fig. 2a). These GNSS data record both long-term motion and various seasonal motions. In order to obtain the actual postseismic deformation caused by the 2012 Indian Ocean earthquake, other deformation should be removed. To do that, we assume that long-term motion can be modeled as a linear trend, and the seasonal effects can be represented by sinusoidal functions. The postseismic deformation can be described by a combination of logarithmic and exponential functions, with τ_{as} and τ_{ve} representing afterslip and viscoelastic decay time, respectively. The full equation for all stations can be written as

$$u(t) = At + B\ln(1 + t/\tau_{as}) + C(1 - e^{-(t/\tau_{ve})}) + D\sin(2\pi t) + E\cos(2\pi t)$$
$$+ F\sin(4\pi t) + G\cos(4\pi t) \tag{1}$$

where t is time (years). We modeled other deformation before the 2012 Indian Ocean earthquake with function (1) and subtracted the pre-earthquake model result from the original observation data. Finally, we obtained the actual postseismic deformation resulting from the 2012 Indian Ocean earthquake (Fig. 2b).

2.2. Finite-element configuration

We compiled geometry to create the finite-element mesh based on previously published models. Surface topography and bathymetry were based on Becker et al. (2009). The subducting slab interface along the Sunda trench was based on the seismic model of Gudmundsson and Sambridge (1998) extrapolated down to our model depth. Earth curvature represented by spherical geometry using local geographically referenced Cartesian system that reflects Earth-Centered Earth-Fixed (ECEF) system. Our model space extended between longitudes 70°E to 115°E and latitudes 20°S to 20°N with a depth of 670 km. The finite-element mesh consisted of more than 5 million tetrahedral elements and contained almost 1 million nodal points. The finest element size was 2.5 km near the source area and the subduction region while rough element size was 100 km at the edge of the model boundary. In order to evaluate the effect of mesh size, we tested with several mesh size (Fig. S1) and concluded negligible effect on our GNSS site (Fig. S2). For simplicity, we set roller conditions at each boundary except for the surface: the surface boundary condition was free displacement. Roller condition means that the model boundaries are fixed in normal direction but free in tangential directions. The mesh is illustrated in Fig. 3.

As the earthquake occurred off the western Sunda trench, but the GNSS stations are on the eastern part of the Sunda trench across the complex subduction region, we incorporated the subducted slab as an elastic overlying plate. Instead of using homogeneous rigidity, we adopted heterogeneous rigidity based on the three-dimensional velocity structure. Inhomogeneity, whether of the stratified layered earth or the heterogeneous earth, has a negligible effect on coseismic deformation (Hashima et al., 2016), but is an indispensable factor for postseismic deformation (Pollitz et al., 2008; Suito and Freymueller, 2009; Wang, 2007; Yoshioka and Suzuki, 1999). We used a three-dimensional velocity structure based on that of Widiyantoro and Van der Hilst (1997).

In this study, the main purpose is to reveal transient rheology structure under the Indian Ocean due to the 2012 Indian Ocean Earthquake. Therefore, to reduce unknown parameter, we assumed several parameters based on previous studies (Fig. 4). Firstly, we fixed elastic thickness on continental side at 65 km as suggested from geodetic (Gunawan et al., 2014) and seismic studies (Wu et al., 2004). Secondly, we assumed continental asthenosphere viscosity as Maxwell body at 9×10^{18} Pa s as a consistent value for subduction zone (Gunawan et al., 2014; Wang, 2007). Also, we set 10^{20} Pa s for both oceanic and continental upper mantle viscosity. Thirdly, we fixed the base of asthenosphere at 220 km and depth of our model at 670 km (Dziewonski and Anderson, 1981).

We conducted finite-element analysis using PyLith code from the Computational Infrastructure for Geodynamics website (https://geodynamics.org/cig/software/pylith/) with a fault interface based on the domain decomposition method (Aagaard et al., 2013b). In PyLith, we adopt bi-viscous Burgers body rheology as a special case of the generalized Maxwell model following Hines and Hetland (2016). The PyLith code has been widely used for crustal deformation modeling such as elastic-viscoelastic modeling (Hines and Hetland, 2016), to study viscoelastic responses (Diao et al., 2013), and also source-inversion modeling using a derived finite-element Green's function (Hsu et al., 2014).

In our model, we used the prescribed slip distribution from Hill et al. (2015) for the Mw 8.6 mainshock and that of Wei et al. (2013) for the
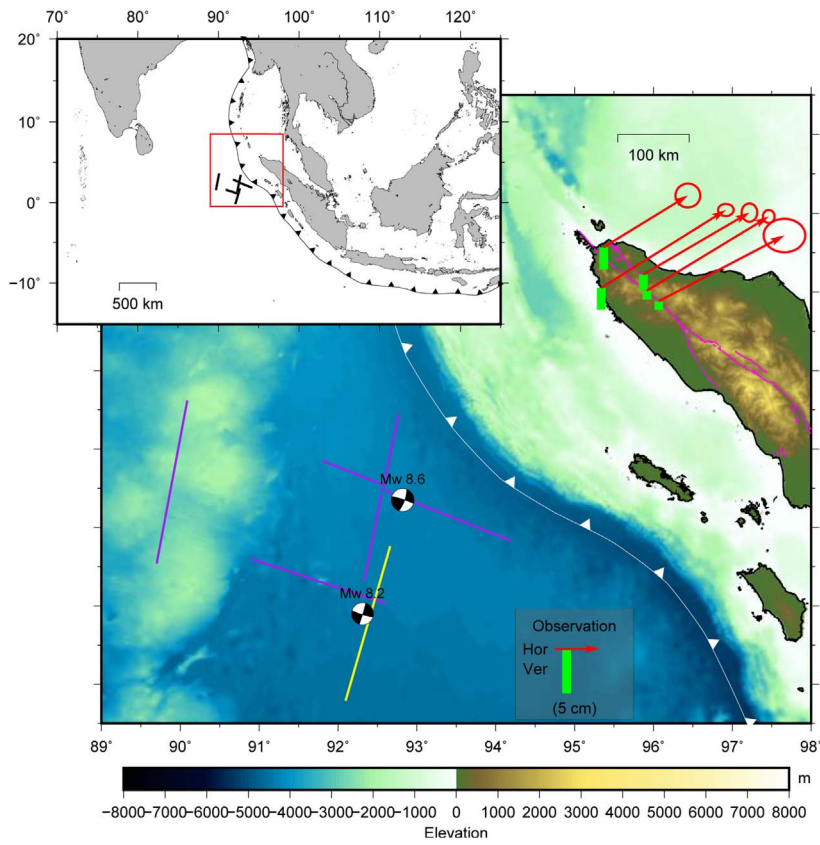
Fig. 1. Red square shows the region of this study. Purple and yellow line indicate fault surface trace due to mainshock Mw 8.6 based on Hill et al. (2015) and largest aftershock Mw 8.2 based on Wei et al. (2013), respectively. Magenta lines in Sumatra Island are Great Sumatran Fault. Red arrows and green bars show horizontal and vertical coseismic offset due to the 2012 Indian Ocean earthquake at GNSS station in northern Sumatra, respectively. White or black lines with triangle represent Sunda trench position based on Gudmundsson and Sambridge (1998). Surface topography and bathymetry are based on Becker et al. (2009). (For interpretation of the references to colour in this figure legend, the reader is referred to the web version of this article.)
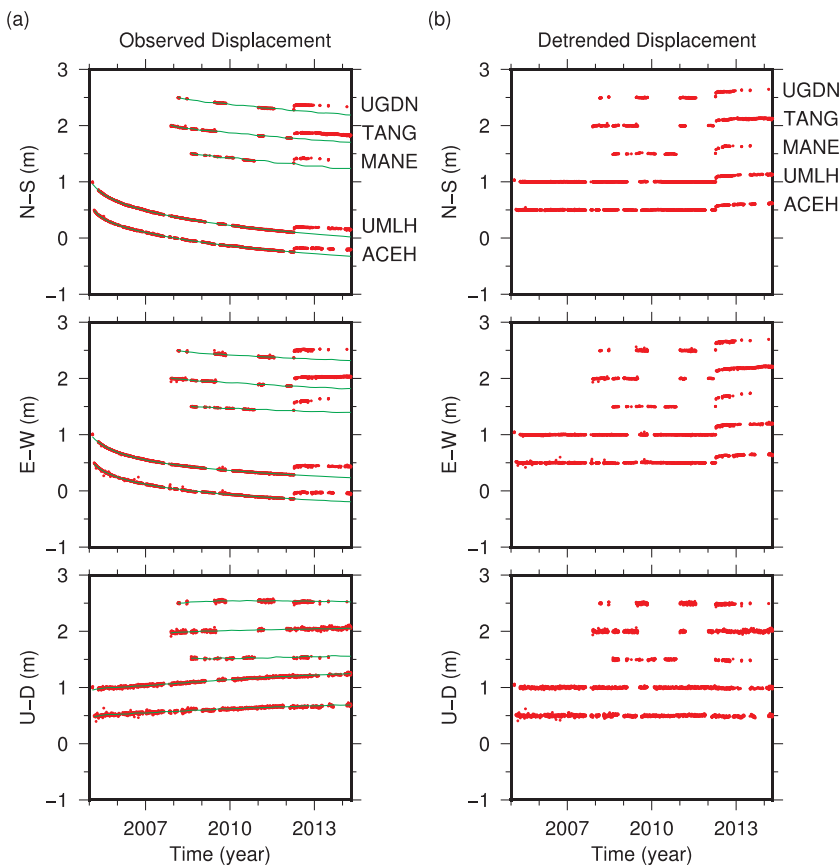

Fig. 2. (a) Observed surface displacement at GNSS station in northern Sumatra for each direction. Red dots show GNSS daily solution from 2005 to 2014.3. Green line represent model displacement fitting using function (1) before 2012 Indian Ocean earthquake (b) Detrended surface displacement after removing pre-earthquake trend based on (a).
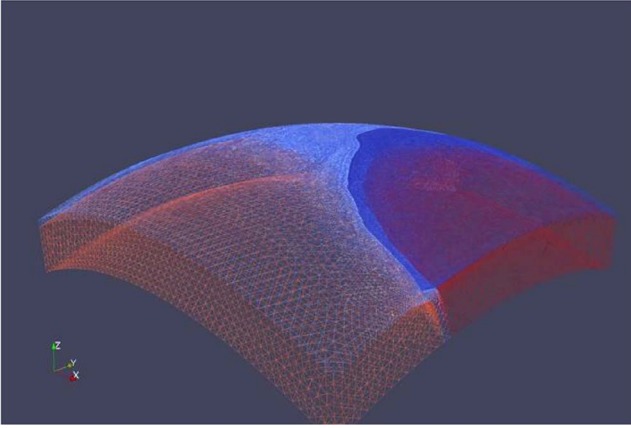
Fig. 3. Model of finite element mesh used in this study. Light blue and blue indicate ocean and continental lithosphere, respectively. While light red and red indicate ocean and continental upper mantle. (For interpretation of the references to colour in this figure legend, the reader is referred to the web version of this article.)

Mw 8.2 aftershock to accommodate our daily solution. Compared with other studies such as Yue et al. (2012) and Wei et al. (2013), the coseismic offset calculated based on Hill et al. (2015) showed better agreement as reported from Gunawan et al. (2016). Forward modeling was used to obtain the surface displacement at each site. Based on this model and two years of GNSS data from northern Sumatra, we obtained estimates of asthenosphere viscosity and lithosphere thickness (Fig. 4).

2.3. Stress-driven afterslip

Afterslip distribution is widely inferred using geodetic inversion (Gunawan et al., 2014; Yamagiwa et al., 2015). However, our geodetic network was limited, sparse, and far from the source; thus, we refrained from inferring the afterslip distribution using geodetic inversion. As our aim was to obtain the surface displacement resulting from afterslip at each GNSS station, we estimated the afterslip based on coseismic stress change. The simulation uses the static stress changes associated with the given coseismic model in a simulation of afterslip governed by static friction law (Aagaard et al., 2013a). Fault surface static stress changing due to the calculated afterslip is equivalent to the fault surface static stress increment due to coseismic slip. In that of sense, the afterslip occurs where the coseismic slip increases the shear tractions. Since this calculation is based on static rupture simulation in order to produce afterslip spatial variation, we additionally need to assume afterslip time variation. Therefore, we modeled the afterslip time evolution by analytical temporal decay function fitting as demonstrated in previous studies (Hu and Wang, 2012; Ohta et al., 2008; Suito and Freymueller, 2009).

There are two main alternatives, which is widely considered: logarithmic and exponential form (e.g. Anugrah et al., 2015; Kreemer et al., 2006). However, as suggested by previous studies (e.g. Ardika et al., 2015; Kreemer et al., 2006), time evolution of afterslip is well explained by logarithmic function than exponential function. Hence, we modeled

the time evolution of afterslip using logarithmic function as following

$$u(t)_n = A_n \ln(1 + t/\tau_{as}) \tag{2}$$

where $u(t)$ and τ_{as} are the surface displacement with spatial-temporal variation and the decay time due to afterslip, respectively. Index n represents each GNSS site. The constant A is a calculated static surface displacement (depend on space) with normalization factor by Euler's number e that is $1/e$ where $e \approx 2.7$. The normalization factor is to ensure that the total afterslip represents slips from the event until fully relaxed.

3. Results

3.1. Afterslip model

The calculated stress-driven afterslip produced subsidence motion at the GNSS network in northern Sumatra, as shown in Fig. 5b. This subsidence has a similar direction to that of the observed coseismic offset in the GNSS network. As we fitted the time evolution of afterslip with a logarithmic function (2), we obtained a decay time due to afterslip of approximately 8.76 days. The estimated decay time indicated that aseismic slip duration due to afterslip was short. This obtained value is plausible compared to various earthquake case studies (Ardika et al., 2015; Freed, 2007; Kreemer et al., 2006) which obtained the decay time after earthquake occurrences less than ten days. In this study, we did not attempt to discriminate between afterslip and viscoelastic relaxation mechanism since the data are not able to distinguish between them.

Coseismic model released large seismic moment at shallow part as shown in Fig. S3a. Since we calculate the afterslip spatial distribution based on shear stress changing due to coseismic stress change, the afterslip occurred on the surrounding region of coseismic slip (Fig. S3b). In order to evaluate the more deep afterslip distribution, we tested with several oceanic lithosphere thicknesses and obtained negligible afterslip effect on our GNSS site for more than 60 km thickness. In that of sense, in the rest of the study, we fixed this estimated surface displacement resulting from afterslip.

3.2. Rheology model

In order to estimate the rheology model, we used a grid search algorithm. We examined three parameters, the thickness of the oceanic lithosphere layer and the asthenosphere viscosity with both Kelvin and Maxwell viscosity, to obtain the minimum chi-squared, χ^2. The chi-squared misfit between the observations and the combined rheology model is as follows:

$$\chi^2 = \sum_{n=1}^{N} \sum_{i=1}^{3} \sum_{t=1}^{T} \frac{(Obs_{n,i,t} - Cal_{visn,i,t} - Cal_{afsn,i,t})^2}{\sigma_{n,i,t}^2} \tag{3}$$

where Obs, Cal_{vis}, and Cal_{afs} are the observed GNSS displacement, calculated viscoelastic model, and calculated afterslip model, respectively. The indices n, i, and t represent the GNSS site, the directional component of crustal deformation, and the time step, respectively. N and T are the total GNSS sites and total time steps, respectively, and σ^2 denotes
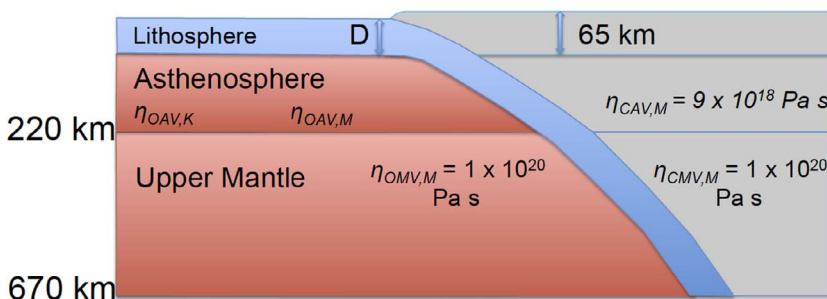

Fig. 4. Model configuration used in this study. Blue color indicates oceanic lithosphere with thickness D. While red colors indicates oceanic upper mantle including asthenosphere layer. Grey color indicates continental side with 65 km lithosphere thickness and 155 km asthenosphere thickness. The depth of our model is 670 km. We abbreviated the estimated viscosity paremeter $\eta_{OAV,K}$ and $\eta_{OAV,M}$ as oceanic asthenosphere Kelvin and Maxwell viscosity, respectively. While $\eta_{OMV,M}$, $\eta_{CMV,M}$ and $\eta_{CAV,M}$ indicate oceanic upper mantle, continental upper mantle and continental asthenosphere viscosity with Maxwell model.
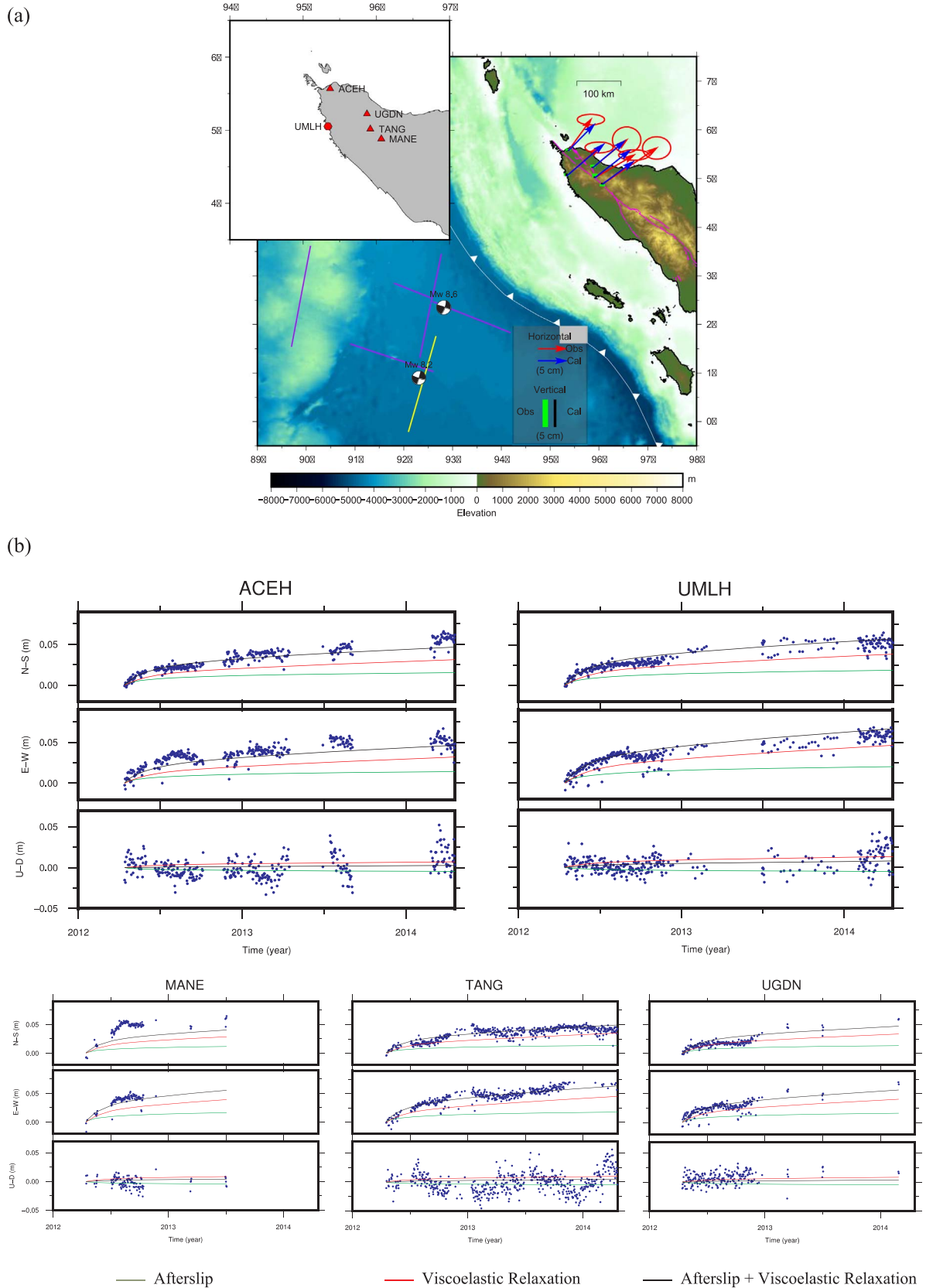
Fig. 5. (a) Red and blue arrows indicate horizontal surface displacement due to 2-years postseismic observation and model, respectively. While green and black bars indicate vertical surface displacement due to 2-years postseismic observation and model, respectively. Red triangle and diamond means GNSS station from AGNeSS and SuGar site, respectively. Fault trace and surface topography/bathymetry description same as Fig. 1. (b) Time series best-fit model for viscoelastic (red line), stress-derived afterslip (green line) and combined model (black line) for each GNSS station within horizontal and vertical direction. Blue dots mean GNSS daily solution from 2012.3 until 2014.3. (For interpretation of the references to colour in this figure legend, the reader is referred to the web version of this article.)
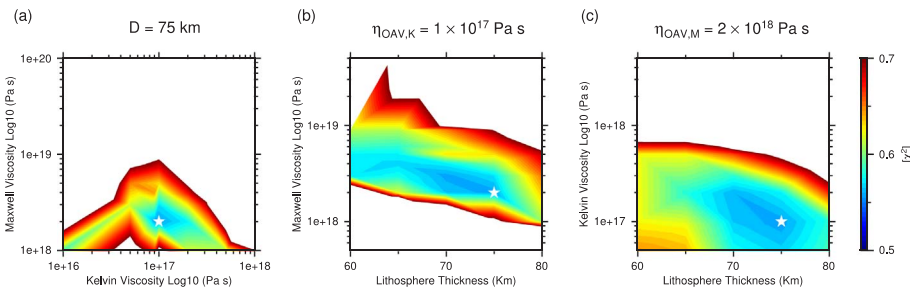
Fig. 6. (a) Trade off between Maxwell viscosity vs Kelvin viscosity, (b) Maxwell viscosity vs lithosphere thickness, (c) Kelvin viscosity vs lithosphere thickness. White star indicates optimum rheology model.

the variance of the GNSS observation for each time step. Both the horizontal and vertical components of the GNSS observations are important. In order to obtain the same contribution both horizontally and vertically, we calculated the misfit value using equal combinations of horizontal and vertical component misfits.

To obtain a more efficient grid search algorithm, we initially searched within a wide, coarse grid for model parameters, subsequently using a finer grid after getting the minimum signal. The minimum misfit for the combined viscoelastic model and afterslip model are illustrated in Fig.6a–c. Based on the grid search results, we obtained an optimum rheology model of 75 km thickness for the oceanic lithosphere, asthenosphere Kelvin viscosity of 1×10^{17} Pa s, and Maxwell viscosity of 2×10^{18} Pa s (Fig.6a). Assuming that afterslip is negligible and thus not including the afterslip in the analysis, we obtained an optimum rheology model with Kelvin viscosity of 5×10^{16} Pa s and Maxwell viscosity of 1×10^{18} Pa s with a thinner oceanic lithosphere (70 km). Although the afterslip model exhibited slight subsidence in the vertical component, which is the opposite sense to the observed postseismic uplift, the misfit value was 13% higher when excluding the afterslip model compared to including the model.

We evaluate the robustness of our result. We calculate optimum model by applying grid search to minimize chi-square misfit value from five scenarios. Each scenario has one site to be removed from analysis. Therefore, we obtained the optimum model based on each scenario on Table 1. The Kelvin and Maxwell viscosity has maximum difference about 1×10^{17} Pa s and 1×10^{18} Pa s., respectively. Meanwhile, the oceanic lithosphere thickness has maximum difference about 5 km. We concluded that our rheology result is robust.

4. Discussion

4.1. Implication of rheology model

We estimated a rheology model consisting of oceanic lithosphere thickness and asthenosphere viscosity with bi-viscous Burgers body rheology. Lithosphere thickness has an important physical relation with rheology, which influences viscoelastic flow. High-temperature, high-pressure creep experiments have suggested that plastic deformation of olivine, which is the most abundant mineral in the mantle, will be

Table 1
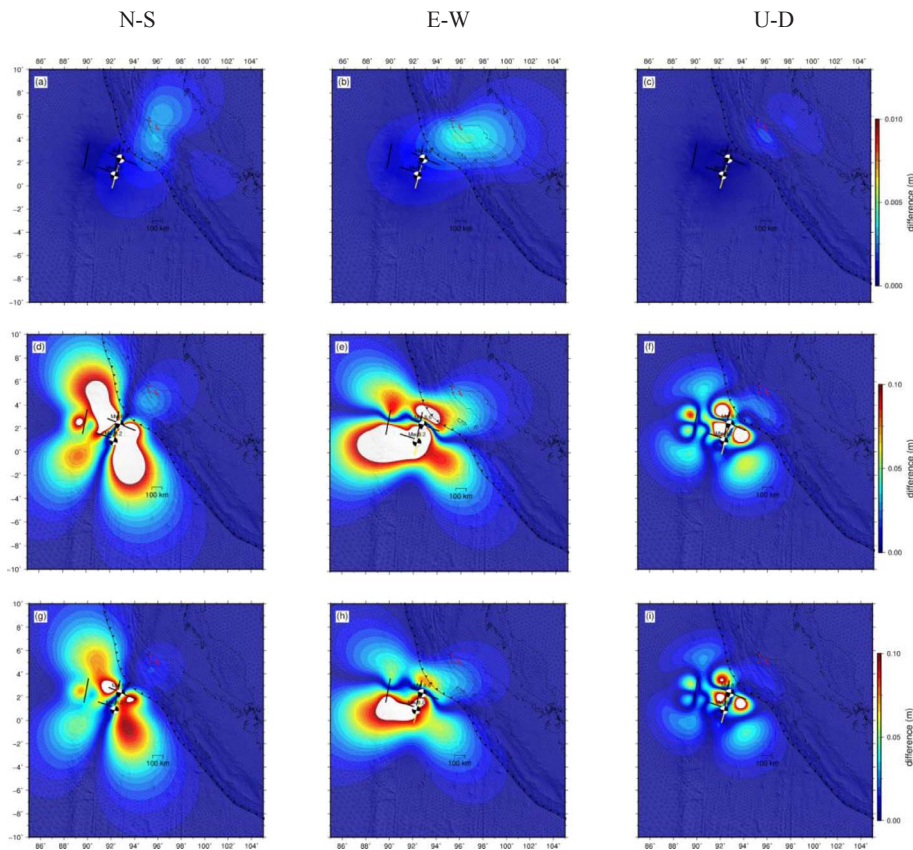Robustness test based on our GNSS data.

Removed site	Optimum model		
	Kelvin viscosity (Pa s)	Maxwell viscosity (Pa s)	Oceanic Lithosphere Thickness (km)
None	1×10^{17}	2×10^{18}	75
ACEH	1×10^{17}	3×10^{18}	70
UMLH	9×10^{16}	2×10^{18}	70
TANG	1×10^{17}	3×10^{18}	70
UGDN	1×10^{17}	3×10^{18}	65
MANE	2×10^{17}	2×10^{18}	70

satisfied by a thermally activated flow law if the temperature reaches 1100–1200 °C (Karato, 2010). Therefore, the effective viscosity above this isotherm must be higher than 1×10^{20} Pa s. As the isotherm is strongly dependent on the age of oceanic lithosphere (McKenzie et al., 2005), and the 2012 Indian Ocean earthquake was located in an oceanic plate with an age of 40–55 Myr (Jacob et al., 2014; Müller et al., 2008), the rigid cold lithosphere must be 70–80 km thick. Our results suggest that the average thickness of the oceanic lithosphere is 75 km, which is consistent with the value derived from thermal structure studies (McKenzie et al., 2005).

In previous studies, Han et al. (2015) and Hu et al. (2016) assumed the thickness of oceanic lithosphere to be 60 and 50 km, respectively. These oceanic thicknesses, based on oceanic thermal structure, should have average temperatures of 1000 °C–1100 °C, meaning that the rock will still have high viscosity. Conversely, within those thicknesses, the age of the oceanic plate should be between 20 and 30 Myr in order to maintain a viscosity lower than 1×10^{19} Pa s. These ages for the 2012 Indian Ocean earthquake region are markedly younger than those obtained by Jacob et al. (2014) and Müller et al. (2008).

The estimated asthenosphere viscosities in this study are 1×10^{17} Pa s for transient Kelvin viscosity and 2×10^{18} Pa s for steady-state Maxwell viscosity with thicknesses of 75 km of oceanic lithosphere and 145 km of oceanic asthenosphere. This result indicates that a weak asthenosphere layer lies below the strong, cold, rigid oceanic lithosphere. Initially, we fixed the continental asthenosphere (mantle wedge) viscosity at 9×10^{18} Pa s following steady-state Maxwell as the average viscosity in the subduction zone (Wang et al., 2012). The assumption of continental asthenosphere viscosity from Hu et al. (2016) is different from this study. Since all of GNSS data that we used are located on the continental side. In order to evaluate the effect of continental asthenosphere viscosity, we calculate magnitude from one order difference of continental viscosity (9×10^{18}–9×10^{19} Pa s) where other parameters were fixed. We carried out this analysis for 2-years period as same period as our observation period. Hu et al. (2016) fixed the viscosity about 3×10^{19} Pa s which is less than one order difference of viscosity. Therefore, we concluded that the effect from continental asthenosphere to our GNSS site is negligible (Fig. 7a–c). Once we can fix continental asthenosphere viscosity, our estimated oceanic rheology indicates that the viscosity of oceanic asthenosphere is lower than that of continental asthenosphere. This result is consistent with previous studies which suggest the lower oceanic asthenosphere viscosity is an important factor for driving plate motion (e.g., Forsyth and Uyeda, 1975).

The estimated viscosity results are almost one order of magnitude lower than those of Han et al. (2015), who obtained values of 1×10^{19} Pa s for steady-state Maxwell viscosity and 1×10^{18} Pa s for transient Kelvin viscosity. This discrepancy may have arisen from different assumptions of the structural model. The model of Han et al. (2015) used a spherical layered earth (Pollitz, 1997), neglecting the effects of the oceanic elastic slab, whereas previous studies (Yoshioka and Suzuki, 1999; Pollitz et al., 2008) pointed out that the slab could significantly affect viscoelastic relaxation. We concluded that the effect of the slab significantly reduced the postseismic uplift at in the fore-arc

and back-arc regions. Thus, to obtain the observed postseismic uplift with a model incorporating an elastic slab, lower viscosity values are required.

The model of Hu et al. (2016) used the same finite-element method as the present study; however, several assumptions of that study were completely different, and their aim was to estimate Maxwell viscosity in the oceanic upper mantle and asthenosphere utilizing middle-field and far-field GNSS data. The primary objective of the present study was to estimate the transient viscosity, as the far-field GNSS dataset does not reflect rapid changes in motion during the early stage of postseismic deformation. Thus, we focused only on constraining the Kelvin viscosity using the middle-field GNSS dataset for northern Sumatra (Fig. 5a), which exhibits transient motion in the first two months (Fig. 5b). Another different assumption is to do with the asthenosphere layer. The Hu et al. (2016) model assumed that the asthenosphere layer subducts following the oceanic lithosphere layer. From rock experiments, mantle flow is mainly controlled by pressure- and temperature-dependent viscosity (Karato, 2010). Therefore, a special mechanism is required to explain the low viscosity values below a depth of 300 km in the Hu et al. (2016) model. Thus, instead of a subducted asthenosphere layer, we adopted layered viscosity with the asthenosphere layer terminating at the trench, as assumed by previous studies (Diao et al., 2013; Pollitz et al., 2008). The Hu et al. (2016) model yielded a low viscosity of approximately 2×10^{18} Pa s with a thin (80 km) asthenosphere layer. In the present study, the estimated asthenosphere viscosity is 2×10^{18} Pa s, similar to that of Hu et al. (2016), but with a greater asthenosphere thickness (145 km). This discrepancy probably results from the different of oceanic asthenosphere geometry and rheology body assumptions.

The viscosity and thickness of the asthenosphere under the ocean are important factors to explain the shear stress induced by plate motion. The plate velocity of the India–Australian plate in the reference frame of the Sunda block is approximately 5 cm/year (Simons et al., 2007; Bock et al., 2003). Assuming that the asthenosphere layer is moving with the oceanic plate and reaches zero velocity at the bottom of the asthenosphere, the shear strain rate in the asthenosphere, $\dot{\varepsilon}_{xy}$, can be written as:

$$\dot{\varepsilon}_{xy} = \frac{v}{2H} \tag{4}$$

where v and H are the plate motion velocity and asthenosphere thickness, respectively. Therefore, the shear stress induced by the plate motion, τ_{xz}, is as follows:

$$\tau_{xz} = 2\eta\dot{\varepsilon}_{xy} = \frac{\eta v}{H} \tag{5}$$

where η is the Maxwell viscosity of the asthenosphere. From this, the total effect of the Hu et al. (2016) model yields a shear stress in the asthenosphere layer induced by plate motion of approximately 0.4 MPa, whereas the result in this study is approximately 0.2 MPa. However, based on Han et al. (2015) model, the estimated shear stress should be 1 MPa. Wiens and Stein (1985) proposed the shear stress induced by the oceanic plate within 5 cm/year should be less than 0.1 MPa. Considering that the shear stress on the asthenosphere is induced by plate motion, our result is the closest value of the three models.

We try to discriminate only the Maxwell body model from the Burgers model; however, the Maxwell model cannot explain the rapid postseismic motion change. Consideration of a less complex viscoelastic model with a straight uni-viscous rheology demonstrates that it reliably underestimates the amplitude of the signal for the first two months. Therefore, coupling of transient and steady-state rheology is required to explain the rapid change in postseismic motion.

The GNSS vertical component is important in this analysis because there may be different trends in the vertical direction but similar trends in the horizontal component. In this case, we only see postseismic uplift in linear features. We supposed that the afterslip relaxation time is rather similar to Kelvin viscoelasticity. Therefore, during the early stage
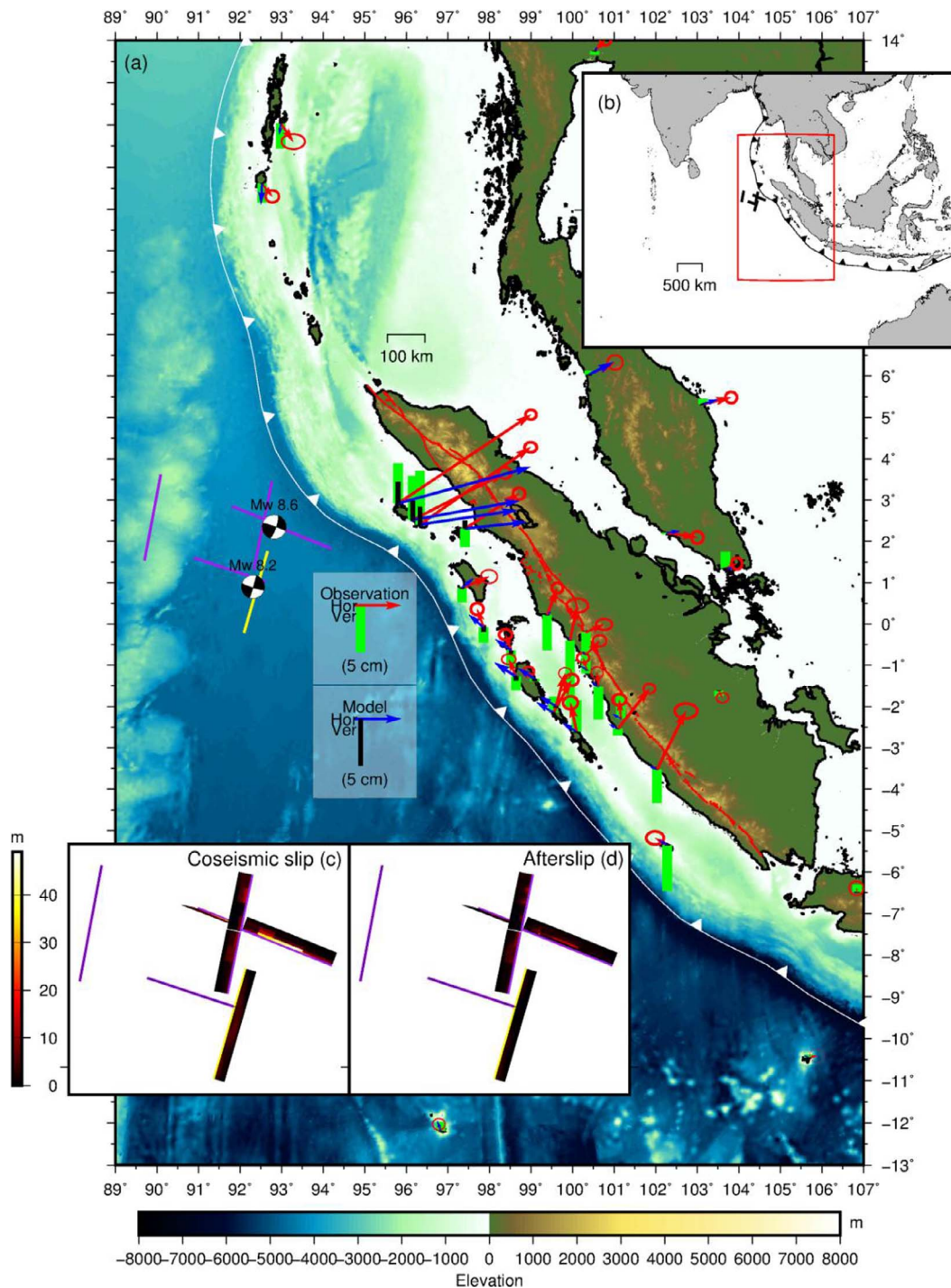
Fig. 8. Fault trace and surface topography/bathymetry description same as Fig. 1. Arrows and bars description same as Fig. 5. (a) Impact of our optimum model for 3-years to other GNSS site provided by Hu et al. (2016). (b) Red square shows the region of (a). (c) Coseismic slip distribution that used in this study. (d) Afterslip distribution obtained from modeling and used for analysis. Fault dip angle on (c) and (d) based on Hill et al. (2015) for Mw8.6 and Wei et al. (2013). The 3-D view of (c) and (d) shown in Fig. S3. (For interpretation of the references to colour in this figure legend, the reader is referred to the web version of this article.)

of postseismic deformation, these two mechanisms canceled each other out, resulting in the Maxwell viscoelasticity controlling the trend of the vertical component. However, in the horizontal component, the afterslip and Kelvin viscoelasticity have a similar direction, which strengthens the displacement magnitude. Hence, coupled afterslip and Kelvin viscoelasticity are essential to explain linear postseismic uplift in the vertical component and rapid change in the horizontal component.

There are previous studies that inferred weak asthenosphere under the ocean in other regions. Weak asthenosphere underlying oceanic

plates has been inferred in different regions such as beneath the North American plate (James et al., 2009) from glacial isostatic adjustment and beneath the Pacific plate (Sun et al., 2014) based on postseismic deformation caused by the 2011 Tohoku-Oki earthquake utilizing in-land and seafloor GNSS data. These results suggest that the viscosity of the oceanic asthenosphere is lower than that of the mantle wedge. James et al. (2009) estimated the depth-dependent viscosity of the asthenosphere beneath the oceanic plate and continental plate. Although the asthenosphere viscosity varied with depth, they determined

that the steady-state viscosity is approximately 3×10^{18} Pa s within 140 km asthenosphere thickness and gradually increases below this layer. In addition, Sun et al. (2014) reported a thin layer at the lithosphere–asthenosphere boundary (at a depth of 45 km) with a viscosity of 2.5×10^{17} Pa s for both transient and steady-state viscosities. In the present study, we obtained transient and steady-state viscosities of approximately 1×10^{17} Pa s and 2×10^{18} Pa s, respectively. These values were estimated using thicknesses of 75 km for the lithosphere layer and 145 km for the asthenosphere layer. Our results are comparable with those of other studies of the asthenosphere (James et al., 2009; Sun et al., 2014).

4.2. Impact to surrounding region

We calculate our optimum model comprises of 75 km oceanic lithosphere thickness, asthenosphere Kelvin viscosity 1×10^{17} Pa s and Maxwell viscosity 2×10^{18} Pa s at GNSS site of surrounding region obtained from Hu et al. (2016). As we can see on Fig. 8, in general, our model could explain horizontal magnitude almost in all sites. However, similar to Hu et al. (2016) result, the observed direction of horizontal velocities of middle field GNSS data in fore-arc region tends to be rotated counterclockwise from the model by 10–20 degree. Since fully relaxed deformation is identical regardless of viscosity value, changing the viscosity value only changes rate of postseismic deformation and does not alter the direction significantly.

First caused of rotated observed horizontal velocities comes from how Hu et al. (2016) removed the pre-earthquake trend. Since they only used logarithmic function to detrend the GNSS data, it might be insufficient to fit both viscoelastic and afterslip deformation due to several mega-thrust earthquakes. In this study, we used both logarithmic and exponential function to detrend the GNSS data. Second possible caused is due to sudden strengthening of interplate coupling just after the 2012 Indian Ocean earthquake as observed in northeast Japan after interplate thrust earthquake (Heki and Mitsui, 2013). In addition, we conduct sensitivity analysis for oceanic asthenosphere Maxwell viscosity (10^{18} Pa s – 10^{19} Pa s) and Kelvin viscosity (10^{17} Pa s – 10^{18} Pa s) as has been done for continental asthenosphere viscosity. We found that GNSS site at fore-arc region has negligible effect due to oceanic viscoelastic relaxation than our GNSS site in northern Sumatra (Fig. 7d-i). In addition, GNSS site at fore-arc region was dominated by northward motion due to interplate coupling (Bradley et al., 2016).

The magnitude of vertical model on middle field GNSS site at fore-arc region in this study is larger than Hu et al. (2016) model even after we include afterslip that slightly subsidence. Coseismic dependency may play a role since our coseismic model based on Hill et al. (2015), which released the largest seismic moment at shallow part (Fig. 8c). On the other hand, Hu et al. (2016) used Wei et al. (2013) coseismic model that released the largest seismic moment at middle part of fault surface.

The previous study such as Hu et al. (2016) constrained lower bound estimate of the steady-state viscosity using middle-field and far-field GNSS data. However, Hu et al. (2016) failed to explain middle-field GNSS data. Based on our sensitivity analysis (Fig. 7d–i), middle field GNSS data is strong constrained for both transient and steady-state viscosity. Therefore, we concluded that our GNSS data is sufficient to discriminate Kelvin and Maxwell viscosity.

The rheology modeling in this study used several simplifying assumptions. We assumed sharp boundaries between the lithosphere, asthenosphere, and upper mantle with uniform viscosity in each mantle layer. Also, we assumed uniform thickness for oceanic lithosphere while in nature may have spatial variation due to age dependency. Those heterogeneities should be considered in further research. The results of this study provide initial results to constrain the transient viscosity of the oceanic asthenosphere based on GNSS data obtained after the 2012 Indian Ocean earthquake.

5. Conclusions

We studied the rheology of the asthenosphere based on postseismic deformation resulting from the 2012 Indian Ocean earthquake utilizing GNSS data in northern Sumatra obtained within two years from the Mw8.6 and Mw8.2 event. We found that coupled viscoelastic relaxation and afterslip were active after the earthquake sequence. In order to explain the short-term and long-term motion within two years after the earthquake, an oceanic lithosphere thickness of 75 km combined with a low transient viscosity of 1×10^{17} and a Maxwell viscosity of 2×10^{18} Pa s are required. In addition, the best-fit rheology in this study is able to explain the rapid changes in the horizontal component and postseismic uplift features in northern Sumatra within the first two months post-earthquake. The transient Kelvin viscosity and afterslip mainly explain the early stage of postseismic deformation in the first two months. These results clearly reflect the importance of transient rheology of the asthenosphere to explain the observation that affected larger stress due to coseismic stress change. In terms of plate tectonics, these rheological structure results demonstrate the appropriate magnitude of weak asthenosphere as a lubricant layer to maintain the driving force of plate movement.

Appendix A. Supplementary material

Supplementary data associated with this article can be found, in the online version, at http://dx.doi.org/10.1016/j.jseaes.2017.07.049.

References

Aagaard, B.T., Kientz, S., Knepley, M.G., Strand, L., Williams, C., 2013. PyLith User Manual: version 2.1.0. Davis: California: Computational Infrastructure of Geodynamics.

Aagaard, B.T., Knepley, M.G., Williams, C.A., 2013b. A domain decomposition approach to implementing fault slip in finite-element models of quasi-static and dynamic crustal deformation. J. Geophys. Res.: Solid Earth 118, 3059–3079.

Altamimi, Z., Collilieux, X., Métivier, L., 2011. ITRF2008: An improved solution of the international terrestrial reference frame. J. Geodesy 85, 457–473.

Anugrah, B., Meilano, I., Gunawan, E., Efendi, J., 2015. Estimation of postseismic deformation parameters from continuous GPS data in northern Sumatra after the 2004 Sumatra-Andaman earthquake. Earthq. Sci. 28, 347–352.

Ardika, M., Meilano, I., Gunawan, E., 2015. Postseismic deformation parameters of the 2010 M7.8 Mentawai, Indonesia, earthquake inferred from continuous GPS observations. Asian J. Earth Sci. 8, 127–133.

Becker, J.J., Sandwell, D.T., Smith, W.H.F., Braud, J., Binder, B., Depner, J., et al., 2009. Global bathymetry and elevation data at 30 arc seconds resolution: SRTM30_PLUS. Mar. Geodesy 32, 355–371.

Bock, Y., Prawirodirdjo, L., Genrich, J.F., Stevens, C.W., et al., 2003. Crustal motion in Indonesia from Global Positioning System measurements. J. Geophys. Res. 108, 3–17.

Bradley, K.E., Feng, L., Hill, E.M., Natawidjaja, D.H., Sieh, K.E., 2016. Implications of the diffuse deformation of the Indian Ocean lithosphere for slip partitioning of oblique plate convergence in Sumatra. J. Geophys. Res. 121, 572–591.

Dach, R., Hugentobler, U., Fridez, P., Meindl, M., 2007. Bernese GPS Software Version 5.0. User Manual. Astronomical Institute, University of Bern.

Diao, F., Xiong, X., Wang, R., Zheng, Y., Walter, T.R., Weng, H., Li, J., 2013. Overlapping post-seismic deformation processes: Afterslip and viscoelastic relaxation following the 2011Mw 9.0 tohoku (Japan) earthquake. Geophys. J. Int. 196, 218–229.

Dziewonski, A.M., Anderson, D.L., 1981. Preliminary reference Earth model. Phys. Earth Planet. Inter. 25, 297–356.

Forsyth, D., Uyeda, S., 1975. On the relative importance of the driving forces of plate motion. Geophys. J. Roy. Astron. Soc. 43, 163–200.

Freed, A.M., 2007. Afterslip (and only afterslip) following the 2004 Parkfield, California, earthquake. Geophys. Res. Lett. 34.

Gudmundsson, Ó., Sambridge, M., 1998. A regionalized upper mantle (RUM) seismic model. J. Geophys. Res. 103, 7121–7136.

Gunawan, E., Maulida, P., Meilano, I., Irsyam, M., Efendi, J., 2016. Analysis of coseismic fault slip models of the 2012 Indian Ocean earthquake: importance of GPS data for crustal deformation studies. Acta Geophys. 64, 2136–2150.

Gunawan, E., Sagiya, T., Ito, T., Kimata, F., Tabei, T., Ohta, Y., Sugiyanto, D., et al., 2014. A comprehensive model of postseismic deformation of the 2004 Sumatra-Andaman earthquake deduced from GPS observations in northern Sumatra. J. Asian Earth Sci. 88, 218–229.

Han, S.C., Sauber, J., Pollitz, F., 2015. Coseismic compression/dilatation and viscoelastic uplift/subsidence following the 2012 Indian Ocean earthquakes quantified from satellite gravity observations. Geophys. Res. Lett. 3764–3772.

Hashima, A., Becker, T.W., Freed, A.M., Sato, H., Okaya, D.A., 2016. Coseismic deformation due to the 2011 Tohoku-oki earthquake: influence of 3-D elastic structure around Japan. Earth, Planets and Space 68, 159.

Heki, K., Mitsui, Y., 2013. Accelerated pacific plate subduction following interplate thrust earthquakes at the Japan trench. Earth Planet. Sci. Lett. 363, 44–49.

Hill, E.M., Yue, H., Barbot, S., Lay, T., Tapponnier, P., Hermawan, I., et al., 2015. The 2012 Mw 8.6 Wharton Basin sequence: a cascade of great earthquakes generated by near-orthogonal, young, oceanic mantle faults. J. Geophys. Res.: Solid Earth 120, 3723–3747.

Hines, T.T., Hetland, E.A., 2016. Rapid and simultaneous estimation of fault slip and heterogeneous lithospheric viscosity from post-seismic deformation. Geophys. J. Int. 204, 569–582.

Hsu, Y.J., Simons, M., Williams, C., Casarotti, E., 2014. Three-dimensional FEM derived elastic Green's functions for the coseismic deformation of the 2005 Mw 8.7 Nias-Simeulue, Sumatra earthquake. Geochem. Geophys. Geosyst. 12.

Hu, Y., Bürgmann, R., Banerjee, P., Feng, L., Hill, E.M., Ito, T., et al., 2016. Asthenosphere rheology inferred from observations of the 2012 Indian Ocean earthquake. Nature 538, 368–372.

Hu, Y., Wang, K., 2012. Spherical-Earth finite element model of short-term postseismic deformation following the 2004 Sumatra earthquake. J. Geophys. Res. 117, 1–15.

Ito, T., Gunawan, E., Kimata, F., Tabei, T., Simons, M., Meilano, I., et al., 2012. Isolating along-strike variations in the depth extent of shallow creep and fault locking on the northern Great Sumatran Fault. J. Geophys. Res.: Solid Earth 117, 1–16.

Jacob, J., Dyment, J., Yatheesh, V., 2014. Revisiting the structure, age, and evolution of the Wharton Basin to better understand subduction under Indonesia. J. Geophys. Res.: Solid Earth 119, 169–190.

Karato, S.I., 2010. Rheology of the deep upper mantle and its implications for the preservation of the continental roots: a review. Tectonophysics 481, 82–98.

Kreemer, C., Blewitt, G., Maerten, F., 2006. Co- and postseismic deformation of the 28 March 2005 Nias Mw 8.7 earthquake from continuous GPS data. Geophys. Res. Lett. 33.

McKenzie, D., Jackson, J., Priestley, K., 2005. Thermal structure of oceanic and continental lithosphere. Earth Planet. Sci. Lett. 233, 337–349.

Miyazaki, S., Segall, P., Fukuda, J., Kato, T., 2004. Space time distribution of afterslip following the 2003 Tokachi-oki earthquake: implications for variations in fault zone frictional properties. Geophys. Res. Lett. 31, L06623.

Müller, R.D., Sdrolias, M., Gaina, C., Roest, W.R., 2008. Age, Spreading Rates, and Spreading Asymmetry of the World's Ocean Crust. Geochemistry, Geophysics, Geosystems, pp. 9.

Ohta, Y., Miura, S., Iinuma, T., Tachibana, K., Matsushima, T., Takahashi, H., Hasegawa, A., et al., 2008. Coseismic and postseismic deformation related to the 2007 Chuetsu-oki, Niigata Earthquake. Earth, Planets and Space 60, 1081–1086.

Peltzer, G., Rosen, P., Rogez, F., Hudnut, K., 1998. Poroelastic rebound along the Landers 1992 earthquake surface rupture. J. Geophys. Res. 103, 30131.

Pollitz, F., Banerjee, P., Grijalva, K., Nagarajan, B., Bürgmann, R., 2008. Effect of 3-D viscoelastic structure on post-seismic relaxation from the 2004 M = 9.2 Sumatra earthquake. Geophys. J. Int. 173, 189–204.

Satriano, C., Kiraly, E., Bernard, P., Vilotte, J.P., 2012. The 2012 Mw 8.6 Sumatra earthquake: Evidence of westward sequential seismic ruptures associated to the reactivation of a N-S ocean fabric. Geophys. Res. Lett. 39.

Simons, W.J.F., Socquet, A., Vigny, C., Ambrosius, B.A.C., Abu, S.H., Promthong, C., et al., 2007. A decade of GPS in Southeast Asia: Resolving Sundaland motion and boundaries. J. Geophys. Res: Solid Earth 112.

Suito, H., Freymueller, J.T., 2009. A viscoelastic and afterslip postseismic deformation model for the 1964 Alaska earthquake. J. Geophys. Res.: Solid Earth 114.

Sun, T., Wang, K., Iinuma, T., Hino, R., He, J., Fujimoto, H., et al., 2014. Prevalence of viscoelastic relaxation after the 2011 Tohoku-oki earthquake. Nature 514, 84–87.

Wang, K., 2007. Elastic and viscoelastic models of crustal deformation in subduction earthquake cycles. Seismogenic Zone Subduct. Thrust Faults 540–575.

Wang, K., Hu, Y., He, J., 2012. Deformation cycles of subduction earthquakes in a viscoelastic Earth. Nature 484, 327–332.

Wei, S., Helmberger, D., Avouac, J.P., 2013. Modeling the 2012 Wharton basin earthquakes off-Sumatra: complete lithospheric failure. J. Geophys. Res.: Solid Earth 118, 3592–3609.

Wessel, P., Smith, W.H.F., Scharroo, R., Luis, J., Wobbe, F., 2013. Generic mapping tools: improved version released. EOS Trans. AGU 94, 409–410.

Widiyantoro, S., Van der Hilst, R., 1997. Mantle structure beneath Indonesia inferred from high-resolution tomographic imaging. Geophys. J. Int. 130, 167–182.

Wiens, D.A., Stein, S., 1985. Implications of oceanic intraplate seismicity for plate stresses, driving forces and rheology. Tectonophysics 116, 143–162.

Wu, H.H., Tsai, Y.Ben., Lee, T.Y., Lo, C.H., Hsieh, C.H., Toan, D.Van., 2004. 3-D shear wave velocity structure of the crust and upper mantle in South China Sea and its surrounding regions by surface wave dispersion analysis. Mar. Geophys. Res. 25, 5–27.

Yamagiwa, S., Miyazaki, S., Hirahara, K., Fukahata, Y., 2015. Afterslip and viscoelastic relaxation following the 2011 Tohoku-oki earthquake (Mw 9.0) inferred from inland GPS and seafloor GPS/Acoustic data. Geophys. Res. Lett. 42, 66–73.

Yoshioka, S., Suzuki, H., 1999. Effects of three-dimensional inhomogeneous viscoelastic structures on postseismic surface deformations associated with the great 1946 Nankaido earthquake. Pure Appl. Geophys. 154, 307–328.

Yue, H., Lay, T., Koper, K.D., 2012. En échelon and orthogonal fault ruptures of the 11 April 2012 great intraplate earthquakes. Nature 490, 245–249.